

Water Resources Research







RESEARCH ARTICLE

10.1029/2023WR034729

Emergence of Unstable Focused Flow Induced by Variable-Density Flows in Vertical Fractures

Special Section:

Impacts on Water Resources of Coupled Hydrological, Chemical, and Mechanical Processes in the Fractured Subsurface

Hongfan Cao^{1,2}, Seonkyoo Yoon¹ , Zhenyu Xu³, Laura J. Pyrak-Nolte³ , Etienne Bresciani⁴ , and Peter K. Kang^{1,2} 

¹Department of Earth and Environmental Sciences, University of Minnesota, Twin Cities, MN, USA, ²Saint Anthony Falls Laboratory, University of Minnesota, Minneapolis, MN, USA, ³Department of Physics and Astronomy, Purdue University, West Lafayette, IN, USA, ⁴University of O'Higgins, Rancagua, Chile

Key Points:

- The density difference between injected and ambient fluids induces unstable focused flow in vertical fractures
- Flow topology analysis is used to identify vortices that are caused by Rayleigh-Taylor instability
- Fluid inertia controls the instability of the focused flow by affecting the size and movement of vortices, even in laminar flow regimes

Supporting Information:

Supporting Information may be found in the online version of this article.

Correspondence to:

P. K. Kang,
pkkang@umn.edu

Citation:

Cao, H., Yoon, S., Xu, Z., Pyrak-Nolte, L. J., Bresciani, E., & Kang, P. K. (2023). Emergence of unstable focused flow induced by variable-density flows in vertical fractures. *Water Resources Research*, 59, e2023WR034729. <https://doi.org/10.1029/2023WR034729>

Received 3 MAR 2023

Accepted 1 NOV 2023

Author Contributions:

Conceptualization: Laura J. Pyrak-Nolte, Peter K. Kang

Data curation: Hongfan Cao

Formal analysis: Hongfan Cao, Peter K. Kang

Funding acquisition: Laura J. Pyrak-Nolte, Peter K. Kang

Abstract Fluids with different densities often coexist in subsurface fractures and lead to variable-density flows that control subsurface processes such as seawater intrusion, contaminant transport, and geologic carbon sequestration. In nature, fractures have dip angles relative to gravity, and density effects are maximized in vertical fractures. However, most studies on flow and transport through fractures are often limited to horizontal fractures. Here, we study the mixing and transport of variable-density fluids in vertical fractures by combining three-dimensional (3D) pore-scale numerical simulations and visual laboratory experiments. Two miscible fluids with different densities are injected through two inlets at the bottom of a fracture and exit from an outlet at the top of the fracture. Laboratory experiments show the emergence of an unstable focused flow path, which we term a “runlet.” We successfully reproduce the unstable runlet using 3D numerical simulations and elucidate the underlying mechanisms triggering the runlet. Dimensionless number analysis shows that the runlet instability arises due to the Rayleigh-Taylor instability (RTI), and flow topology analysis is applied to identify 3D vortices that are caused by the RTI. Even under laminar flow regimes, fluid inertia is shown to control the runlet instability by affecting the size and movement of vortices. Finally, we confirm the emergence of a runlet in rough-walled fractures. Since a runlet dramatically affects fluid distribution, residence time, and mixing, the findings in this study have direct implications for the management of groundwater resources and subsurface applications.

Plain Language Summary Groundwater systems are often composed of fractured rocks, and the fractures provide major pathways for groundwater flow and mass transport. Fractured rock aquifers account for about 75% of the Earth's near-surface aquifer systems, and fluids with different densities often coexist in subsurface fractures. Thus, understanding the role of variable-density fluids on fracture flows is essential for managing groundwater resources and predicting, designing, and operating many subsurface applications. The effects of density are strongest in vertical fractures; however, most previous studies on flow and transport through fractures are limited to horizontal fractures, and few have investigated the density effects on flow and mixing through vertical fractures. In this study, we report both experimental and numerical evidence of an intriguing, focused flow path caused by a density contrast between two fluids and elucidate the underlying mechanisms triggering the resulting unstable focused flow in vertical fractures, which we name a “runlet.” Further, vortices, which are characterized by rotating flow patterns, are shown to emerge and control the instability of the runlet. Since the runlet dramatically affects fluid distribution, residence time, and mixing, the findings in this study have direct implications for managing groundwater resources and subsurface applications.

1. Introduction

Fractured rock aquifers compose about 75% of the Earth's near-surface aquifer systems (Dietrich et al., 2005) and often contain coexisting fluids with different densities in the fractures. Understanding the role of variable-density fluids on flow, transport, and mixing in fractures is essential to the prediction, design, and operation of many subsurface activities because fractures are the main flow paths in subsurface rocks. As shown in Figure 1, variable-density flows in vertical fractures can commonly occur in fractured geologic media. For example, in coastal fractured aquifers, the denser seawater can preferentially intrude through fractures saturated with freshwater (Park et al., 2012). Thus, understanding variable-density flows in fractures is important for managing water resources in coastal aquifers. Further, magma flow in dykes often involves variable-density flows (Yamato et al., 2012), and variable-density fluid flows also occur during geologic CO₂ or H₂ sequestration, in which

© 2023 The Authors.

This is an open access article under the terms of the [Creative Commons Attribution-NonCommercial License](https://creativecommons.org/licenses/by-nc/4.0/), which permits use, distribution and reproduction in any medium, provided the original work is properly cited and is not used for commercial purposes.

Investigation: Hongfan Cao, Seonkyoo Yoon, Zhenyu Xu, Etienne Bresciani, Peter K. Kang

Methodology: Hongfan Cao, Seonkyoo Yoon, Zhenyu Xu, Etienne Bresciani, Peter K. Kang

Project Administration: Peter K. Kang

Resources: Laura J. Pyrak-Nolte, Peter K. Kang

Software: Hongfan Cao, Seonkyoo Yoon

Supervision: Peter K. Kang

Validation: Peter K. Kang

Visualization: Hongfan Cao

Writing – original draft: Hongfan Cao

Writing – review & editing: Seonkyoo Yoon, Laura J. Pyrak-Nolte, Etienne Bresciani, Peter K. Kang

Resources: Laura J. Pyrak-Nolte, Etienne Bresciani, Peter K. Kang

injected less dense CO₂ or H₂ tends to migrate upwards and can leak through fractures (Tongwa et al., 2013). The leakage of CO₂ or H₂ can lead to serious consequences such as jet fire, unconfined vapor cloud explosion, and toxic chemical release (Portarapillo & di Benedetto, 2021). Variable-density flows in channels are not limited to geophysical flows; they are also very common in various industrial applications in the field of biochemical and materials engineering. Chemical samples and biological materials with different densities are often transported in channel flows in applications of these fields (Günther & Jensen, 2006; Morijiri et al., 2011). Therefore, understanding density effects on transport and mixing in channel flows is critical for the prediction, design, and operation of various applications.

Many previous studies have shown that density contrast has a significant impact on flow and solute transport in fractures (Graf & Therrien, 2005, 2007; Shikaze et al., 1998). An experimental study by Tenchine and Gouze (2005) showed that even a weak density contrast between two fluids, coupled with fracture wall roughness effects, can create preferential solute transport paths and stagnation zones that result in anomalously long tails in breakthrough curves. Even without fracture wall roughness, density contrasts have been shown to impact the flow and transport of solutes in a horizontal straight channel (Bouquain et al., 2011). Such density effects on flow and solute transport may dramatically increase when a fracture is inclined or vertical, which is common in nature. For example, Ronen et al. (1995) showed that a slight density contrast can dramatically change tracer breakthrough curves in vertical conduit flows. However, few studies have investigated density effects on the flow and transport of variable-density fluids in vertical fractures.

Further, variable-density fluid flow affects fluid mixing, which can in turn affect dissolution and precipitation patterns (Chaudhuri et al., 2009; Simmons, 2005; Tsang & Neretnieks, 1998). For example, in CO₂-brine injection experiments conducted by Ott and Oedai (2015), the mixing of CO₂ and brine formed carbonic acid that dissolved carbonate minerals. The study found that the dissolution occurred preferentially in the lower part of the horizontally oriented rock sample. Snippe et al. (2017) explained that in Ott and Oedai's experiments, gravity effects played an important role in determining the zone of preferential mixing and dissolution. Other studies, such as Oltéan et al. (2013), investigated buoyancy-driven dissolution in a vertical fracture and reported the geometrical changes of dissolution patterns over a wide range of Péclet, Damköhler, and Richardson numbers. A follow up study (Ahoulou et al., 2020) elucidated that the dissolution patterns were controlled by the level of density contrast. The density effects on mixing, dissolution, and precipitation would be much stronger in vertical fractures. However, most previous studies focused on variable-density fluid flow in porous media or horizontal fractures, and density effects on mixing and transport in vertical fractures have been elusive.

In particular, density effects may induce flow instability, which affects fluid flow, transport, and mixing. For example, the experiment on dissolution in inclined rectangular blocks showed that the dissolution patterns were affected by flow instability due to density stratification (Cohen et al., 2020). This example highlights that flow instability caused by density contrast can be critical in fracture flows. Different mechanisms have been proposed to explain the origin of instability in variable-density flows (Almarcha et al., 2010; Fernandez et al., 2002; Kneafsey & Pruess, 2010; Trevelyan et al., 2011; Wooding et al., 1997; Zalts et al., 2008). The most common explanation is Rayleigh-Taylor instability (RTI). In RTI, the displacement at the interface between two miscible fluids of different densities can lead to unstable density stratifications and fingering patterns due to gravity and buoyancy effects generated by concentration gradients. Another well-known situation that can lead to flow instability is Kelvin-Helmholtz instability (KHI). KHI occurs when there is a sufficient velocity difference across the interface between two fluids. However, the leading mechanisms triggering flow instability in vertical fractures with variable-density fluids remain unclear.

In this study, we report both experimental and numerical evidence of an intriguing, focused flow path caused by a density contrast between two fluids and investigate the underlying mechanisms triggering the resulting unstable focused flow in vertical fractures. Three-dimensional (3D) numerical simulations are conducted for a wide range of controlling factors, including density contrast, flow rate, solute diffusivity, and fracture roughness. Flow topology analysis is conducted to analyze the complex 3D flow fields and to identify the locations and number of vortices that control the instability of focused flow. Further, dimensionless number analysis is used to elucidate the underlying mechanisms triggering the observed instability, and we extend the findings to a rough fracture.

The remainder of this article is organized as follows. The experiment and simulation setups are detailed in Section 2. The results are given and discussed in Section 3. In Section 4, we summarize our key findings and conclusions.

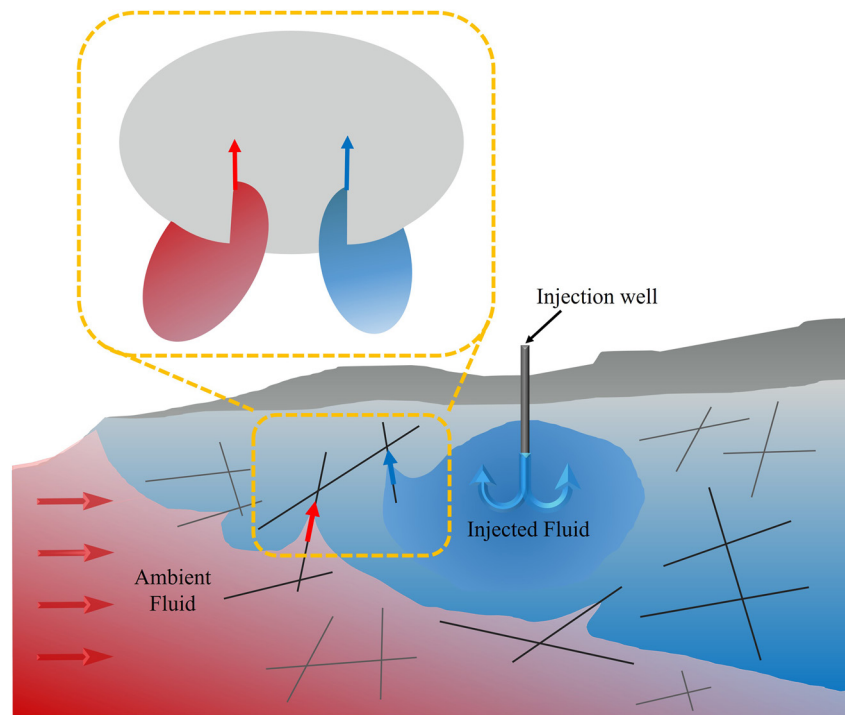


Figure 1. Schematic diagram of a common scenario where a vertical fracture is intersected by two other fractures that introduce fluids with distinctive properties into the vertical fracture. In three-dimensional (3D) fracture networks, such a scenario (two different fluids flowing into a fracture through two other fractures that intersect the fracture) is very likely to occur.

2. Methods

2.1. Experimental and Numerical Simulation Setup

Fracture flow is often simplified as the flow between two parallel flat plates, known as Hele-Shaw flow (Al-Bahlani & Babadagli, 2012; Chen, 1989; Saffman & Taylor, 1958). In this study, we start with a vertical flow cell with parallel flat plates and then extend the findings to rough fractures. A Hele-Shaw cell is an idealized but good proxy for identifying critical flow and fluid-related factors that affect variable-density flow and solute transport in a vertical fracture. For visual laboratory experiments, we used two flat transparent polycarbonate sheets (100 mm × 100 mm × 12.7 mm) separated by spacers to form a fracture with a uniform aperture of 4 mm. Two nonreactive miscible fluids with different densities (Fluid 1 and Fluid 2) were introduced through two inlets at the bottom of the fracture and exited through a single, elongated outlet at the top of the fracture (Figures 2a and 2b). The size of the two inlet ports was 3 mm × 3 mm, and the rectangular outlet port was 3 mm × 60 mm. The two inlets were placed 38 mm apart at the bottom of the system. The fluid and flow-related conditions used in the laboratory experiment are identical to the reference case (Case 1) shown in Table 1. The denser fluid (Fluid 1) was composed of Na₂CO₃, NaCl, and water, and Fluid 1 was injected through the left inlet port. The lighter fluid (Fluid 2) was composed of Na₂CO₃ and water, and was introduced through the right inlet port. The addition of NaCl in Fluid 1 was to make the density difference between the two fluids. The denser fluid (Fluid 1) also contained a dye (Brocresol green) to enable the imaging of fluid distributions, and a RaspberryPi spy camera was used for digital imaging. Readers are referred to Xu et al. (2023) for additional experimental details.

Numerical simulations were used to investigate the effects of density contrasts, injection rates, diffusion, and fracture roughness on variable-density flows in a vertical fracture. Figure 2c shows the simulation setup that is based on the laboratory experimental setup, and Figure 2d provides a simulated image of the concentration distribution, in which the concentration value is proportional to Fluid 1 concentration. The entire domain was discretized into 400 × 400 × 16 cells where each cell is a cube of edge length 0.25 mm. All domain boundaries were set to no-slip boundaries except for the inlets and outlet. The inlets are set as a fixed flow rate condition while the outlet is set as a fixed pressure condition. We simulated a total of 14 cases to study the effects of density

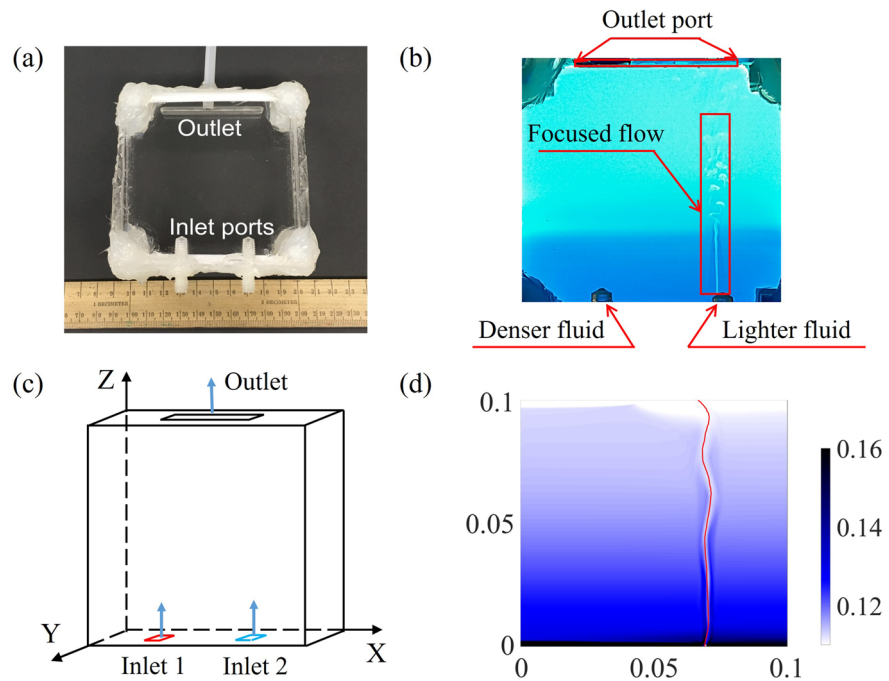


Figure 2. (a) Experimental setup used in the laboratory experiment. (b) A snapshot from a laboratory experiment. The fracture aperture is 4 mm, the injection rate is 0.17 ml/min for lighter fluid, 1.36 ml/min for denser fluid, and the density ratio is 1,111/1031.8. (c) Setup and boundary conditions of the numerical model. (d) A snapshot of depth-averaged concentration distribution obtained from the numerical simulation of Case 1. Concentration values represent the normalized concentration of Fluid 1 where the maximum concentration after the normalization is 1. The maximum concentration in the colorbar is set to 0.16 to better show the runlet shape and the higher concentration around the runlet. The injection rates and the fluid properties are identical to the laboratory experiment.

contrasts, injection rates, diffusion, and roughness. Table 1 lists the fluid and flow-related parameters for all the numerical cases. The reference case (Case 1) refers to the case in which the conditions were identical to those in the laboratory experiment. The parameters that differ from the reference case are shown in boldface.

The experimental and numerical setup mimics a common situation where a vertical fracture is intersected by two other fractures that introduce fluids with distinctive properties into the vertical fracture (Figure 1). In 3D fracture networks, such a scenario (two different fluids flowing into a fracture through two other fractures that intersect the fracture) is very likely to occur (e.g., Bochet et al., 2020). The mixing of fluids in fractures is relevant to engineered subsurface systems in fractured aquifers where the injection and withdrawal of fluids occur, such as in aquifer storage and recovery (ASR), carbon mineralization, and geothermal systems. In these applications, an exogenic fluid is injected into a groundwater system. The injected fluid typically has a density and velocity that is distinct from the ambient groundwater. Thus, in a typical field setting where there is a background flow of an ambient fluid, the injection of a less dense fluid can lead to the coexistence of two fluids with different densities in a fracture. Our experimental setup realized the coexistence of two fluids in a simple yet effective way. Specifically, our study design resulted in a situation where a lighter fluid is flowing more dominantly through a vertical fracture. The injection of the denser fluid with a smaller flow rate mimics the background fluid flow, and the setup allows the system to reach a quasi-steady state where the two fluids coexist. If we inject only the less dense fluid, the system will eventually be fully occupied by the injection fluid. The most dynamic fluid-rock interactions will occur in fractures that have the coexistence of two different fluids over a long time, and the study design allows one to investigate such a situation.

2.2. Governing Equations and Numerical Solution

3D pore-scale numerical simulations are conducted to study the variable-density flow and transport of miscible fluids of different densities in a vertical fracture. Fluid flow in a fracture can be described by the Navier-Stokes (N-S) equations that consider the mass and momentum conservations

Table 1
Fluid and Flow-Related Parameters Used in the Numerical Study Cases

		Density (kg/m ³)	Injection rate (ml/min)	Diffusion coefficient (m ² /s)	Péclet number
Case 1 (reference case)	Fluid 1	1,111	0.17	10 ⁻⁹	10 ⁴
	Fluid 2	1031.8	1.36		
Case 2	Fluid 1	1031.8	0.17	10 ⁻⁹	10 ⁴
	Fluid 2	1031.8	1.36		
Case 3	Fluid 1	1,040	0.17	10 ⁻⁹	10 ⁴
	Fluid 2	1031.8	1.36		
Case 4	Fluid 1	1,073	0.17	10 ⁻⁹	10 ⁴
	Fluid 2	1031.8	1.36		
Case 5	Fluid 1	1186.6	0.17	10 ⁻⁹	10 ⁴
	Fluid 2	1031.8	1.36		
Case 6	Fluid 1	1289.8	0.17	10 ⁻⁹	10 ⁴
	Fluid 2	1031.8	1.36		
Case 7	Fluid 1	1,111	0.17	10⁻⁶	10
	Fluid 2	1031.8	1.36		
Case 8	Fluid 1	1,111	0.17	10⁻⁷	100
	Fluid 2	1031.8	1.36		
Case 9	Fluid 1	1,111	0.17	10⁻⁸	10 ³
	Fluid 2	1031.8	1.36		
Case 10 (noninertial)	Fluid 1	1,111	0.17	10 ⁻⁹	10 ⁴
	Fluid 2	1031.8	1.36		
Case 11	Fluid 1	1,111	0.17	10 ⁻⁹	1.26 × 10 ³
	Fluid 2	1031.8	0.17		
Case 12 (rough fracture)	Fluid 1	1031.8	0.17	10 ⁻⁹	10 ⁴
	Fluid 2	1031.8	1.36		
Cases 13 and 14 (rough fracture)	Fluid 1	1,111	0.17	10 ⁻⁹	10 ⁴
	Fluid 2	1031.8	1.36		

Note. Fluid 1 and Fluid 2 have the identical kinematic viscosity of 1.08×10^{-6} (m²/s) for all cases. Péclet number is defined as $\frac{ul}{D}$ where l is the fracture aperture, u is the maximum injection velocity, and D is the diffusion coefficient.

$$\frac{\partial \rho}{\partial t} + \nabla \cdot (\rho u) = 0 \quad (1)$$

$$\frac{\partial(\rho u)}{\partial t} + \nabla \cdot (\rho u u) = -\nabla p + \rho g + \rho \nu \nabla^2 u \quad (2)$$

where u is the velocity field, p is the pressure field, ρ is the fluid density, g is the gravitational acceleration, and ν is the kinematic viscosity. Solute transport in a fracture is described by the advection-diffusion equation (ADE)

$$\frac{\partial C}{\partial t} + \nabla \cdot (uC) - D \nabla^2(C) = 0 \quad (3)$$

where C is the normalized solute concentration in Fluid 1 (denser fluid) and D is the diffusion coefficient. Thus, the concentration is one when the fluid is composed purely of Fluid 1 (denser fluid), and the concentration is zero when the fluid is composed purely of Fluid 2 (lighter fluid).

Since the density variability in our system arises due to the two miscible fluids with different densities, the fluid density ρ can be expressed as a linear function of concentration C

$$\rho = \rho_0 + \frac{\partial \rho}{\partial C}(C - C_0) \quad (4)$$

where C_0 is the reference concentration of the lighter fluid which we set to be zero, and ρ_0 is the reference density at the reference concentration. Thus, Equations 2 and 3 are coupled through Equation 4 in a nonlinear way: the change of concentration distribution affects the fluid density, which in turn affects the flow field.

The N-S equations are nonlinear partial differential equations. The convective terms in the governing equations involve the multiplication of variables, such as velocity and density, resulting in the nonlinearity of the system. To reduce the nonlinearity, we applied the Boussinesq approximation (Gartling & Hickox, 1985; Gray & Giorgini, 1976). By neglecting density variations in the convective terms, the governing equations become quasilinear. The Boussinesq approximation is valid when the density variability is small and when the gravity force term in the momentum equation is significantly larger than the inertia term, which is the case of this study (Hamimid et al., 2021; Huang et al., 2020). Even with the Boussinesq approximation, some simulations took several weeks using computation resources at Minnesota Supercomputing Institute (MSI). Thus, the Boussinesq approximation was essential for investigating multiple numerical scenarios that we pursued in this study. With the Boussinesq approximation, Equations 1 and 2 can be simplified to

$$\nabla \cdot u = 0 \quad (5)$$

$$\frac{\partial u}{\partial t} + \nabla \cdot (uu) = -\frac{\nabla p}{\rho_0} + \frac{\rho}{\rho_0}g + \nu \nabla^2 u \quad (6)$$

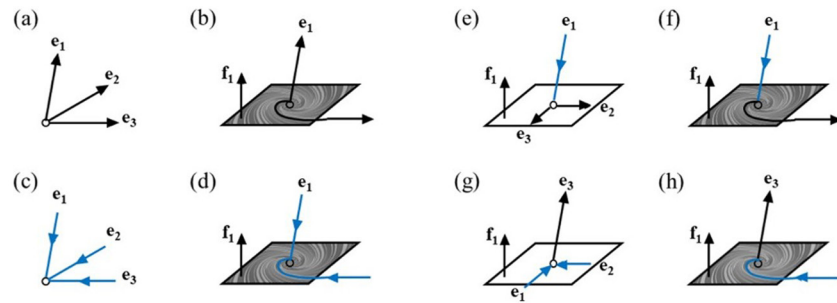
We solve Equations 5 and 6 for fluid flow, Equation 3 for transport, and flow and transport equations are coupled through Equation 4.

We used OpenFOAM (Weller et al., 1998), an open-source CFD software developed by OpenCFD Ltd to perform numerical simulations. `buoyantBoussinesqPimpleFoam` is a flow solver that solves the N-S equations for incompressible flow with the Boussinesq approximation. We coupled the `buoyantBoussinesqPimpleFoam` with a solver for ADE (`scalarTransportFoam`). The flow and transport equations are coupled through the fluid density term that is a function of solute concentration. In summary, fluid flow that honors concentration-dependent density is solved by `buoyantBoussinesqPimpleFoam`, and solute transport and mixing that determines the fluid density field is solved by `scalarTransportFoam`. The maximum Reynolds number ($Re = \frac{ul}{\nu}$) considered in this study is around 10, which is obtained using the fracture aperture as l and the maximum injection velocity as u . This indicates that the flow is in the laminar regime (Wood et al., 2020), and thus we set the simulation type to be laminar in the OpenFOAM input file.

2.3. Flow Topology Analysis

Various flow topologies can emerge in 3D velocity fields (Bakker & Berger, 1991; Détery, 2013; Perry & Chong, 1994; Romanò et al., 2017). In particular, the flow fields of variable-density flows can be complex and thus challenging to characterize (Bresciani et al., 2019; Contreras et al., 2017; Hidalgo & Dentz, 2018; Lee & Kang, 2020; Stein et al., 1989). A powerful way to analyze complex 3D velocity fields is by identifying and tracking the essential structures of a flow field using the concept of vector field topology (Asimov, 1993; Globus et al., 1991; Helman & Hesselink, 1989; Perry & Fairlie, 1975; Theisel et al., 2008). Vector field topology reduces flow complexity through the identification of the topological features of the flow field (e.g., stagnation points, dividing stream surfaces), which constitutes the backbone of a flow field. Moreover, tracking these topological features over time or over a change in system parameters provides insight into the dynamics of the system (Chiogna et al., 2015; Cirpka et al., 2015; de Barros et al., 2012; Lester et al., 2009; Theisel et al., 2005).

Stagnation points constitute key information about a flow field and thus the identification of stagnation points is an important step in the topology analysis. For a 3D vector field $v(x)$, a stagnation point x_0 is extracted by finding $v(x_0) = 0$ with $v(x_0 \pm \epsilon) \neq 0$ (where ϵ is an arbitrarily small quantity) and is classified based on the eigenvalues λ_i ($i = 1..3$) of the Jacobian matrix of the 3D vector field $J(x_0)$. Depending on the sign of the real parts of the eigenvalues $Re(\lambda_i)$, the stagnation points can be classified into four nondegenerate types: sources, sinks, repelling saddles, and attracting saddles



Sources and sinks: (a) repelling node; (b) repelling focus; (c) attracting node; (d) attracting focus. Repelling and attracting saddles: (e) Repelling node saddle; (f) repelling focus saddle; (g) attracting node saddle; (h) attracting focus saddle.

Figure 3. Eight common types of stagnation points in three-dimensional (3D) vector fields (modified from Weinkauff (2000)). Repelling focus saddle (f) and attracting focus saddle (h) type stagnation points are associated with vortices, and thus we identify those stagnation points in this study.

$$\text{Sources : } 0 < \text{Re}(\lambda_1) \leq \text{Re}(\lambda_2) \leq \text{Re}(\lambda_3)$$

$$\text{Repelling saddles : } \text{Re}(\lambda_1) < 0 < \text{Re}(\lambda_2) \leq \text{Re}(\lambda_3)$$

$$\text{Attracting saddles : } \text{Re}(\lambda_1) \leq \text{Re}(\lambda_2) < 0 < \text{Re}(\lambda_3)$$

$$\text{Sinks : } \text{Re}(\lambda_1) \leq \text{Re}(\lambda_2) \leq \text{Re}(\lambda_3) < 0$$

Degenerate types only arise rarely (Perko, 2001), and so they are disregarded. The flow patterns around the four types of stagnation points are fundamentally different. Sources and sinks consist of outflow and inflow, respectively. A repelling saddle has one direction of inflow and two directions of outflow, while an attracting saddle has one direction of outflow and two directions of inflow. Each of these types can be further divided into two types according to the imaginary parts of the eigenvalues $\text{Im}(\lambda_i)$

$$\text{Focus : } \text{Im}(\lambda_1) = 0 \text{ and } \text{Im}(\lambda_2) = -\text{Im}(\lambda_3) \neq 0$$

$$\text{Nodes : } \text{Im}(\lambda_1) = \text{Im}(\lambda_2) = \text{Im}(\lambda_3) = 0$$

Note that here and above, the numbering of the eigenvalues does not matter. For the focus type, there is a rotating pattern in the inflow or outflow plane, whereas for the node type, the flow lines are asymptotically straight when approaching the stagnation point. These eight types of 3D stagnation points are visualized in Figure 3. In this study, we identify focus saddle type stagnation points, which are associated with vortices (Figures 3f and 3h). We relied on a VTK-based open-source code to identify the stagnation points and their type (Bujack et al., 2021).

3. Results and Discussion

3.1. The Origin of the Runlet

In the laboratory experiments, the fracture sample was initially filled with the lighter fluid (Fluid 2). Then, simultaneously, the denser fluid (Fluid 1) was continuously injected from the left inlet, and the lighter fluid (Fluid 2) was continuously injected from the right inlet. The two fluids mixed in the fracture and exited through a constant pressure outlet. Experimental results show that the lighter fluid was confined to a narrow path in a vertical fracture. The narrow path is not straight and the shape of the narrow path continuously changes in time (Figure 2b). In this paper, we term the narrow path of the lighter fluid as a “runlet” and denote the continuous change (fluctuation) of runlet shape as the “runlet instability.” The numerical result of the reference case is shown in Figure 2d. The concentration values were averaged in the aperture direction to obtain the depth-averaged concentration field and normalized by the maximum concentration. The simulation successfully reproduces the key features of the experimental results such as the formation of the runlet and the instability of the runlet (Figure 2d). However, small-scale features such as the mushroom-shaped lighter fluid parcels observed in the experiment (runlet in the lighter blue region in Figure 2b) are not evident in the simulation results. To test the effect of mesh resolution,

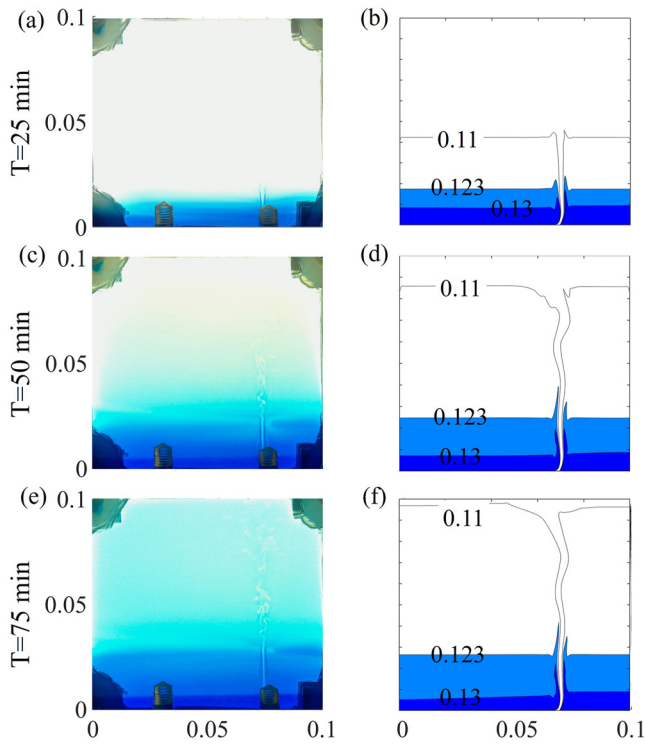


Figure 4. Comparison of experimental and numerical results of the reference case. (a) Experimental result after 25 min of fluid injection. (b) Simulation result after 25 min of fluid injection. (c) Experimental result after 50 min of fluids injection. (d) Simulation result after 50 min of fluid injection. (e) Experimental result after 75 min of fluid injection. (f) Simulation result after 75 min of fluid injection.

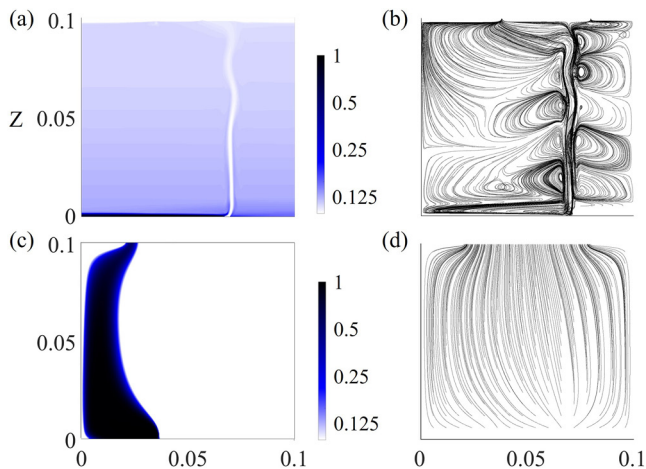


Figure 5. (a) Depth-averaged concentration distribution of Case 1 (the two fluids have different densities). The lighter fluid is confined to a runlet. Note that the colorbar shows the entire concentration range (0–1) but in log scale. (b) Three-dimensional (3D) streamlines of Case 1. The streamlines clearly visualize the runlet and the emergence of vortices along the runlet. (c) Depth-averaged concentration distribution of Case 2 (the two fluids have the same density). (d) 3D streamlines of Case 2. Note that in both cases, the injection rate of Fluid 2 (right inlet) is larger than the injection rate of Fluid 1 (left inlet).

we simulated the reference case using grids with different resolutions and chose the optimum mesh resolution of $0.25 \text{ mm} \times 0.25 \text{ mm} \times 0.25 \text{ mm}$ ($400 \times 400 \times 16$ cells). Using supercomputing resources at MSI, it took about 10 days to run one case using 128 cores and 400 GB RAM. Refining the mesh resolution by twice did not make any noticeable change, but the computation time increased significantly. Due to the stochastic nature of instability, noise in physical experiments, and the limitation of numerical simulation, one cannot capture all the features observed in the experiments such as the detailed ripples around runlet. Figure 4 shows the comparison of experiment and simulation of reference case (Case 1) at different times of fluid injection. The concentration contour lines of $C = 0.11$, $C = 0.123$, and $C = 0.13$ at three different times nicely show good correspondence to the laboratory experiment. Thus, the numerical simulation is capable of reproducing key features such as runlet evolution and runlet instability, which are the focus of this study. In particular, concentration values are higher around the runlet compared to the background concentration both in the experiment and the simulation, which we discuss further in Section 3.3.

In both the laboratory experiments and numerical simulations, the lighter fluid was confined by the denser fluid. To confirm the domain size effect, we also simulated a case with a larger domain size of $150 \text{ mm} \times 150 \text{ mm}$ and confirmed that the key features of runlet remained the same. Therefore, the general conclusion of the study is independent of the domain size. We hypothesize that the density contrast between the two fluids causes the runlet. To test this hypothesis, we simulated Case 2, where the experimental conditions are identical to the reference case but without the density contrast (Table 1). In other words, two fluids with different densities are injected in the reference case, while two fluids with the same density are injected in Case 2, i.e., $\frac{\partial \rho}{\partial C} = 0$. Figure 5 shows the concentration distributions and projected 3D streamlines from the two simulation cases (Please also refer to Movie S1). From the concentration distribution of the reference case (Figure 5a), we can clearly observe that the lighter fluid is confined to an unstable runlet. Whereas in Case 2, there is no runlet (Figure 5c), and the streamlines are smooth and relatively straight (Figure 5d). The larger injection rate of Fluid 2 causes Fluid 2 to occupy more space compared to Fluid 1, and there is limited mixing between the two fluids, as shown by the segregation of the fluids. This demonstrates that the density difference between the two injected fluids underpins the formation of the unstable runlet in the vertical fracture and also strongly affects the overall fluid mixing.

To further study the effects of density contrast on the formation runlet, we simulated four cases with different levels of density contrast (Cases 3–6 in Table 1) and compared them with the reference case (Case 1). Larger α means the density changes more with the same concentration difference, which means the two fluids have a larger density difference. Figure 6 shows the projected concentration distributions and 3D streamlines of the reference case and Cases 3–6. For Case 3 with the smallest α , although we can clearly see the runlet, the runlet was stable and did not fluctuate (Figure 6a). In addition, from the streamlines of Case 3 (Figure 6b) we could identify two stable vortices near the inlet. For all the other cases, the runlets were unstable, more vortices occurred around the runlet, and the vortices traveled upwards along the runlet. The instability of the runlet increased as α increased. These results confirm that the formation and instability of the runlet are strongly affected by the density contrast between the fluids. Density contrast between the lighter fluid and the background fluid should be large enough to sustain the narrow runlet and to induce vortical flows.

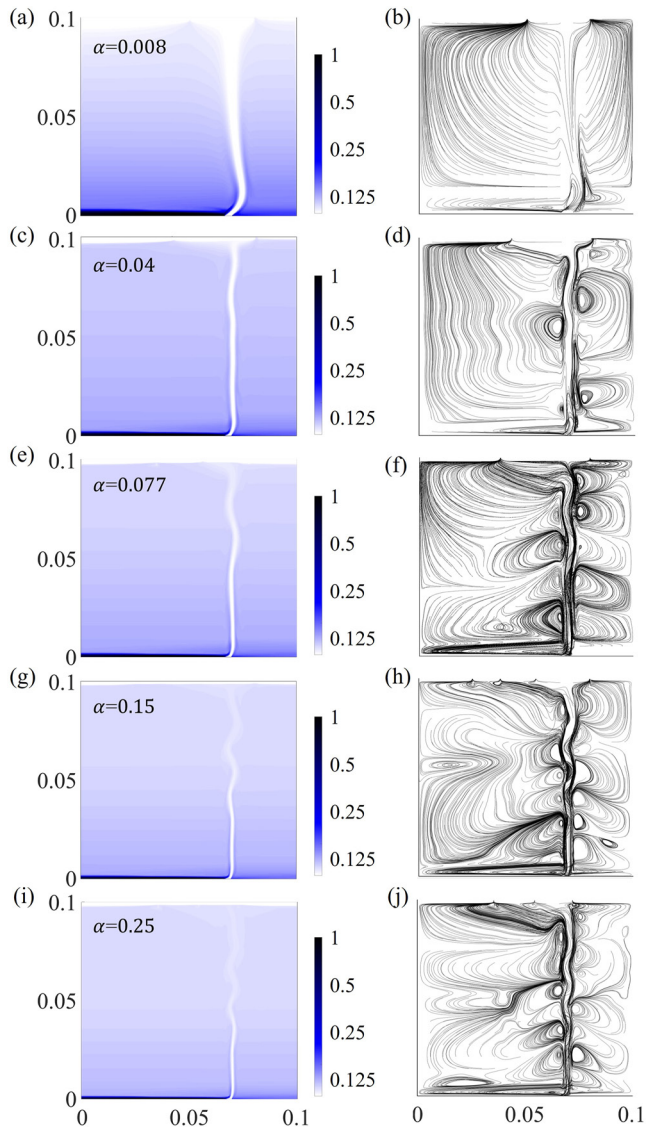


Figure 6. (a) Depth-averaged concentration distribution of Case 3 ($\alpha = 0.008$). (b) Projected three-dimensional (3D) streamlines of Case 3. (c) Depth-averaged concentration distribution of Case 4 ($\alpha = 0.04$). (d) Projected 3D streamlines of Case 4. (e) Depth-averaged concentration distribution of Case 1 (reference case; $\alpha = 0.077$). (f) Projected 3D streamlines of Case 1. (g) Depth-averaged concentration distribution of Case 5 ($\alpha = 0.15$). (h) Projected 3D streamlines of Case 5. (i) Depth-averaged concentration distribution of Case 6 ($\alpha = 0.25$). (j) Projected 3D streamlines of Case 6.

From the concentration distribution shown in Figure 5a, we find that the interface between the lighter and denser fluids is not sharp. The diffused interface of two fluids in the reference case (Case 1) is caused by the active mixing between the two fluids along the runlet. While in the Case 2 (Figure 5c), there is limited mixing between the two fluids, as shown by the segregation of the fluids. Mixing will reduce the density difference between the runlet and background fluid, and the runlet may disappear for enhanced mixing conditions. The mixing between two fluids is controlled by fluid stretching and diffusion (Dentz et al., 2011; Le Borgne et al., 2013; Yoon et al., 2021). Fluid stretching due to velocity heterogeneity is known to control mixing by controlling the length elongation and width compression of the mixing zone near the fluid interface. Vortices that appear near the runlet seem to enhance fluid stretching, and diffusion ultimately mixes the two fluids. If the diffusion coefficient is larger, the mixing of the two fluids will be enhanced, and the density gradient between the runlet and background fluid will decrease, which may lead to the eventual disappearance of the runlet. To study the effects of mixing on the density contrast and the runlet formation, we considered three cases with different diffusion coefficients (Cases 7–9 in Table 1) and compared the results with the reference case. If the density contrast is the origin of runlet formation, it is expected that the runlet will not form or will dissipate for high enough diffusion coefficients. The diffusion coefficient is 10^{-9} [m^2/s] in the reference case and was varied from 10^{-6} to 10^{-8} [m^2/s] in Cases 7 to 9.

Several measures that quantify the mixing state of a system exist, such as interface deformation (de Anna et al., 2013), scalar dissipation (Le Borgne et al., 2010), and dilution index (de Barros et al., 2012; Kitanidis, 1994). Here, we present the dilution index, which effectively quantifies the mixing state over the domain of interest. The dilution index is given by

$$E(t) = \exp\left(-\int c(x, t) \log[c(x, t)] dx\right) \quad (7)$$

where $c(x, t)$ is the normalized concentration. The dilution index is a global measure of dilution, which is integrated over the domain of interest. Figure 7 shows the evolution of dilution index in time for the cases with different diffusion coefficients and the case without density difference (Case 2). The dilution index of Case 2 (dashed line) is significantly smaller than other cases, and this indicates that the runlet significantly increases the overall mixing state of the system. Also, the dilution index increases as the diffusion coefficient increases, which indicates that the two fluids mix more efficiently for a higher diffusion coefficient. Stronger mixing will lead to a decrease in the density gradient between the runlet and the background fluid, and may limit the formation and instability of the runlet.

The concentration distributions and projected 3D streamlines of Cases 7–9 are shown in Figure 8. For Case 7 with the highest diffusion coefficient of 10^{-6} [m^2/s], the two fluids mix well, leading to the disappearance of the runlet (Figure 8a). For Case 8, in which the diffusion coefficient is 10^{-7} [m^2/s], the runlet is visible near the inlet, but it is relatively short and stable (Figure 8c). From the streamlines in Figure 8d, we observe that the vortical flows are only present near the inlet, and then the streamlines disperse rapidly. For Case 9 (Figures 8e and 8f), in which the diffusion coefficient is smaller, we clearly observe an unstable runlet, but there are fewer vortical flow structures than in the reference case (Figures 8g and 8h) which has the smallest diffusion coefficient. These results confirm that the formation of the runlet and the presence of vortical flows along it are strongly affected by the mixing of the two fluids. Only when the diffusion coefficient is small enough, the density contrast between the lighter fluid and the background fluid is large enough to sustain the narrow runlet and to induce vortical flows.

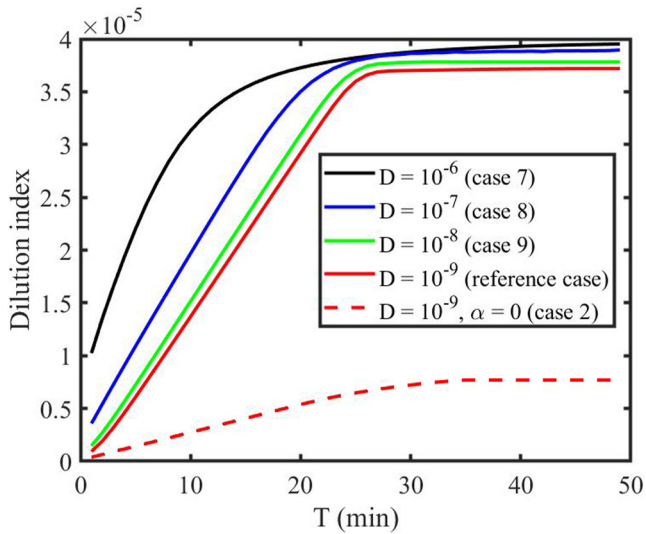


Figure 7. The evolution of dilution index in time. The red line for reference case (Case 1, $D = 10^{-9}$ [m²/s]), the black line for Case 7 ($D = 10^{-6}$ [m²/s]), the blue line for Case 8 ($D = 10^{-7}$ [m²/s]), the green line for Case 9 ($D = 10^{-8}$ [m²/s]), and the red dash line for Case 2 (without density difference).

3.2. Runlet Instability and Flow Topology Analysis

As defined in Section 3.1, the runlet instability means the fluctuation and the continuous change of runlet shape in time. To quantify the level of fluctuation of the runlet, we identified the centerline along the runlet by identifying the location of the minimum concentration on each horizontal x - y plane and tracing those points in the vertical direction (the red line in Figures 2d and 9b). Note that we discretized the domain into 400 horizontal layers with a thickness of 0.25 mm. We define the traced line of minimum concentration as the centerline of the runlet, and the length of the centerline represents the length of the runlet. We can then track the length of the runlet in time. Figure 9a shows the change in the length of the centerline (runlet) in time. We observe that the length of the centerline increases roughly linearly in time and then asymptotes to a constant value. This indicates that the runlet becomes longer and unstable over time and eventually reaches a quasi-steady state where the instability does not intensify further nor dissipate. At the quasi-steady state, the runlet continues to fluctuate as shown in Movie S1.

From the streamlines of the reference case (Figure 5b), we observe that a number of vortices occur along the runlet. Critical stagnation points associated with the vortices were extracted using a topology analysis tool (Bujack et al., 2021). We analyzed the focus saddles (Figures 3f and 3h) because the spiral flow around these stagnation points has the same flow pattern as vortices. The identified focus saddles are shown with blue circles in Figure 9b.

Most of them are indeed located at the center of vortices or near the vortices. Thus, the number of focus saddles is an indicator of the number of vortices. The stagnation points are densely populated near the inlet, and the number decreases in the vertical (flow) direction. In other words, more vortices exist near the lower part of the system, which is also where the concentration gradients are higher. High concentration gradients at the lower part of the system may lead to RTI (Kull, 1991; Sharp, 1984), and the vortices produced by RTI may be the origin of the runlet instability. The relation between RTI, vortices, and runlet instability will be further discussed in the following section.

The spiral flows around vortices affect the flow pattern around the runlet, bending the runlet and leading to the instability of runlet. To check if the vortices are playing a crucial role in causing the runlet instability, we calculated the total number of focus saddles and plotted the total number of these stagnation points over time. The trends of the number of stagnation points and that of the length of the centerline are almost identical (Figure 9a). This result suggests that the number of stagnation points, especially the number of focus saddles, can be used to quantify the instability of the runlet, and the instability of the runlet is strongly affected by the vortices.

3.3. Origin of Runlet Instability: RTI Versus KHI

Here, we investigate the origin of the vortices that control the instability of the runlet over time. Vortical flows can be generated by either concentration gradients or velocity gradients in our system. The concentration and velocity distribution at multiple horizontal cross-sections (at $z = 25$ mm, 50 mm, and 75 mm from the bottom of the domain) at three pore volume injection (PVI) are shown in Figure 10. One PVI is equivalent to the time required for the injected fluid volume to reach the total pore volume of the fracture domain (pore volume divided by injection rate). From the concentration maps (Figures 10a, 10c, and 10e), a large concentration gradient around the runlet is evident. In particular, the concentration at the perimeter of the runlet is higher than that in other areas, showing the nonmonotonic concentration profile. Note that during injection, the denser fluid sinks to the bottom of the fracture due to gravitational effects, displacing the lighter fluid that initially filled the fracture. As both fluids are continuously pumped into the fracture, the denser fluid occupies most of the fracture near the inlet, except where the runlet is. The runlet is formed by the injected lighter fluid, thus having a low concentration. The runlet has a high velocity because the lighter fluid is flowing through a narrow runlet. Thus, the denser fluid near the runlet moves along with the lighter fluid due to the shear drag exerted by the high-velocity runlet flow. This explains the maximum fluid concentration at the perimeter of the runlet, which is also observed in the experiment.

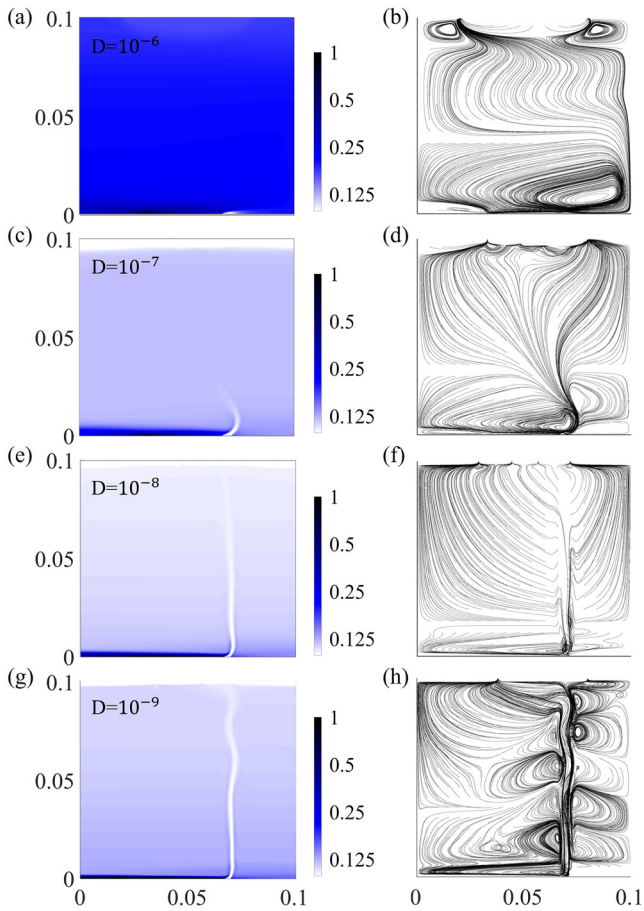


Figure 8. (a) Depth-averaged concentration distribution of Case 7 ($D = 10^{-6} \text{ m}^2/\text{s}$). (b) Projected three-dimensional (3D) streamlines of Case 7. (c) Depth-averaged concentration distribution of Case 8 ($D = 10^{-7} \text{ m}^2/\text{s}$). (d) Projected 3D streamlines of Case 8. (e) Depth-averaged concentration distribution of Case 9 ($D = 10^{-8} \text{ m}^2/\text{s}$). (f) Projected 3D streamlines of Case 9. (g) Depth-averaged concentration distribution of Case 1 ($D = 10^{-9} \text{ m}^2/\text{s}$; reference case). (h) Projected 3D streamlines of Case 1.

The instability of the interface between two fluids caused by different densities is known as RTI (He et al., 1999; Kull, 1991; Sharp, 1984; Tryggvason, 1988). Here, we qualitatively describe the overall process induced by RTI and quantitatively confirm the discussed processes in the following sections. The density contrast between the runlet and surrounding fluid can lead to opposing flow directions between the denser and lighter fluids. At an early stage, the denser fluid at the bottom of the fracture and near the runlet is pulled along the runlet because of the injection force (Figure 11I). This is due to the drag force exerted on the surrounding denser fluid by the fast-flowing lighter fluid. Then, due to the density effect, the denser fluid sinks to the bottom of the fracture and mixes with the surrounding fluid causing RTI. This is how a rotating flow pattern (vortex) emerges at the bottom of the fracture (Figure 11II). Subsequently, the vortex moves upward due to the drag force along the runlet, and the runlet bends due to the spiral flows (Figure 11III). The upward movements of vortices are shown in Movie S1. As the vortex rises, the same phenomenon occurs on the other side of the runlet and another vortical flow emerges. Thus, vortices emerge on either side of the runlet, leading to the runlet bending in alternating directions (Figure 11IV). Figure 11 is a schematic showing the step-by-step process.

The Rayleigh (Ra) number is a dimensionless number that is commonly used to predict and describe the instability of variable-density flows. Ra is the ratio comparing the convective mass transfer and the diffusive mass transfer. When Ra is greater than some critical Rayleigh number, Ra_c , the density-driven convective transport is dominant, and the spiral vortical flows result from the RTI (Cengel et al., 2001; Le Quere, 1990; Solano et al., 2022). The critical Rayleigh number allows us to predict the occurrence of RTI, and the specific value is dependent on a given experimental setup. We quantify Ra using the following definition that is based on the concentration gradient (Hage & Tilgner, 2010; Ślęzak et al., 2004):

$$Ra = \frac{g\alpha l^4}{D\nu} \frac{\partial C}{\partial s} \quad (8)$$

where $\frac{\partial C}{\partial s}$ is the concentration gradient and $\alpha = -\frac{1}{\rho} \frac{\partial \rho}{\partial C}$ describes the density change with regard to concentration. We estimated Ra along the z -direction for different diffusion coefficients (reference case and Cases 7–9 in Table 1).

The representative length l of the fluid volume is taken to be half of the fracture aperture (2 mm). The entire domain is divided into 400 horizontal layers where each layer has the size of 100 mm \times 0.25 mm \times 4 mm. Ra is then calculated for each horizontal subdomain and then plotted along the vertical direction. In each subdomain, the

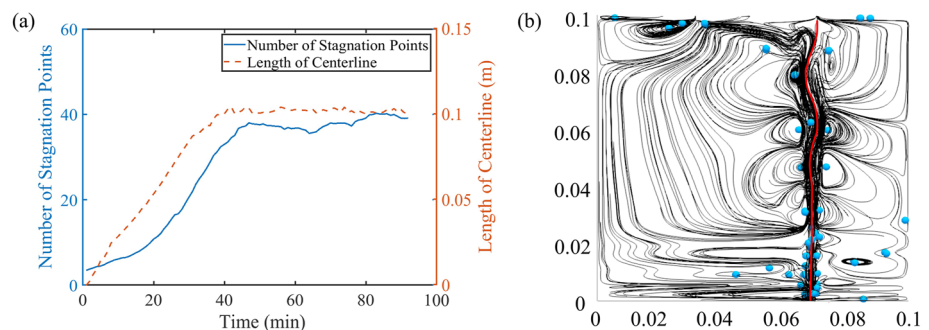


Figure 9. (a) Number of focus saddles (repelling or attracting) and length of the centerline as a function of time. (b) Location of focus saddles at a snapshot of the reference case. Blue circles show the location of identified focus saddles, and the red line shows the centerline.

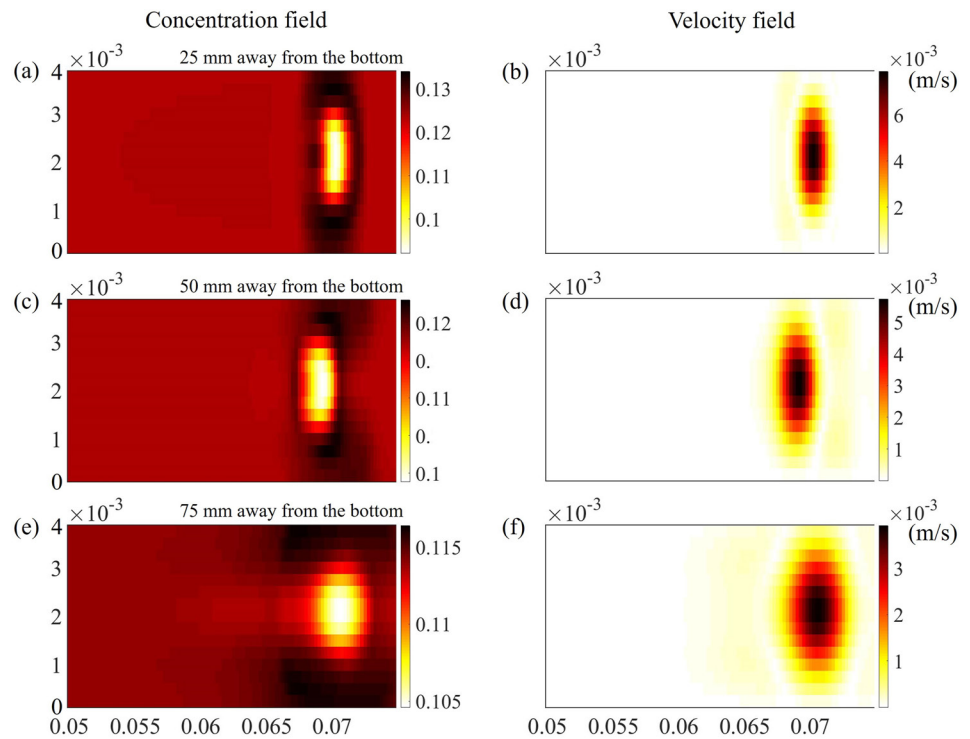


Figure 10. Concentration and velocity fields in cross-sections at (a and b) 25 mm, (c and d) 50 mm, and (e and f) 75 mm from the bottom of the domain. Concentration around the runlet is higher than in other areas. Velocity is greatest at the runlet center.

locations of the maximum and minimum concentration values are identified. Then, ∂C is obtained by taking the concentration difference between these two points, and ∂s is obtained by estimating the distance between the two points.

Figure 12a shows the evolution of Rayleigh number (Ra) as a function of vertical location (z) for cases with different diffusion coefficients, the red line for reference case (Case 1, $D = 10^{-9}$ [m²/s]), the black line for Case 7 ($D = 10^{-6}$ [m²/s]), the blue line for Case 8 ($D = 10^{-7}$ [m²/s]), and the green line for Case 9 ($D = 10^{-8}$ [m²/s]). As shown in Figure 12a, Ra decreases as the diffusion coefficient increases because stronger diffusion leads to a reduced concentration difference. For the case in which the diffusion coefficient is 10^{-7} [m²/s] (red line), the maximum Ra is $\sim 7 \times 10^5$, and when the diffusion coefficient is 10^{-8} [m²/s] (green line), the maximum Ra is $\sim 1.3 \times 10^6$.

Considering that the runlet is stable in the case with a diffusion coefficient of 10^{-7} [m²/s] (red line), and the runlet becomes unstable in the case for a diffusion coefficient of 10^{-8} (green line), we can infer that the instability emerges when Ra is somewhere between 7×10^5 and 1.3×10^6 (the gray zone in Figure 12a). Therefore, the critical Rayleigh number (at which the runlet becomes unstable) is in the order of 1×10^6 .

Figure 12b shows the evolution of Rayleigh number (Ra) as a function of vertical location (z) for cases with different α . The red line shows the reference case where $\alpha = 0.077$. At smallest α of 0.008, the runlet was observed but it was stable, and the system showed runlet instability at $\alpha = 0.04$. Therefore, we can infer that the instability emerges when Ra is somewhere between 5×10^5 and 1.1×10^6 , indicated by the gray zone in Figure 12b. The range of the critical Ra is consistent with what we obtained from the cases with different diffusion coefficients (Figure 12a). Combining these results, we can limit the range of critical Ra to be between 7×10^5 and 1.1×10^6 .

For the cases with the unstable runlet, Ra is larger than Ra_c only near the inlet. This implies that the vortices, which control the instability, can only

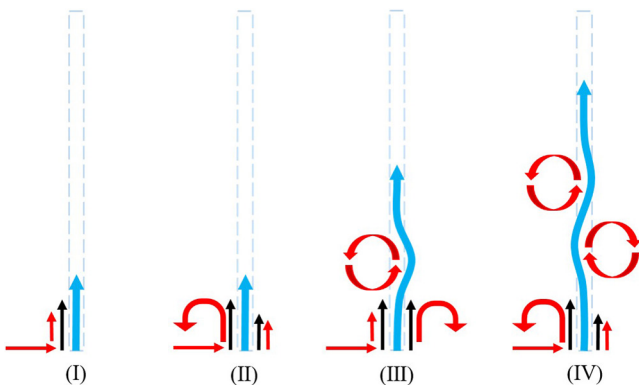


Figure 11. Developmental stages of vortices and unstable runlet. Blue arrows show the movement of the lighter fluid, black arrows show drag force exerted on the denser fluid by the runlet, and red arrows show the movement of the denser fluid.

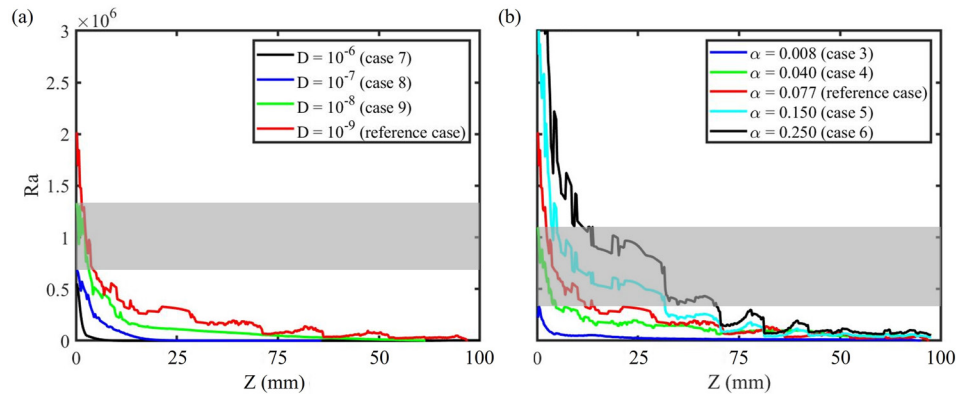


Figure 12. (a) Evolution of Rayleigh number (Ra) as a function of vertical location (z) for cases with different diffusion coefficients. $z = 0$ mm is at the bottom of the fracture (where the inlet is located). (b) Evolution of Rayleigh number (Ra) as a function of vertical location (z) for cases with different α . The critical Ra is within the Ra range indicated by the gray zones.

originate near the lower part of the system. Indeed, it can be observed from Figure 9a that most of the vortices are located near the injection port. Although the Ra at the upper part of the system is smaller than Ra_c , the vortices can travel upwards with the flow because of the injection force and lead to the bending and instability of the runlet. Movie S1 confirms that the instability in the upper part is governed by the vortices that migrated from the bottom part. Traditionally, when the Rayleigh number is larger than critical Rayleigh number, instability sets in and convection cells appear. However, the appearance of convection cells, which we call vortex in this study, does not necessarily mean the runlet instability in our system. Ra should be larger than Ra_c such that it allows the upward movement of vortices, which leads to the instability of runlet.

Another well-known mechanism that can lead to flow instability is the KHI (Funada & Joseph, 2001; Smyth & Moum, 2012). KHI occurs when there is a sufficient velocity difference across the interface between two fluids. The large velocity shear can induce instability along the interface. Therefore, the interface becomes an unstable vortex sheet. From the velocity fields at different cross-sections (Figures 10b, 10d, and 10f), we observe a rapid change in the velocity magnitude near the runlet, which may lead to KHI. For KHI, the Richardson number (Ri) is the dimensionless number that is used to predict the instability. Ri represents the ratio of the buoyancy term to the flow shear term

$$Ri = \frac{g}{\rho} \frac{\frac{\partial \rho}{\partial s}}{\left(\frac{\partial u}{\partial s}\right)^2} \quad (9)$$

where $\frac{\partial u}{\partial s}$ is the velocity gradient. When the Richardson number is below the critical Richardson number Ri_c , the fluid becomes unstable. In other words, the fluid flow should be stable if Ri of the system is significantly larger than Ri_c . Therefore, we estimate the minimum Ri that our system can reach. If the minimum Ri is much larger than Ri_c , we can conclude that the KHI is not the cause of the instability. To obtain the smallest Ri that can occur in our system, we estimate the largest velocity difference ∂u . The maximum velocity difference possible in our system is the injection velocity. Thus, the maximum ∂u is taken as the injection velocity, which is around 2.5 mm/s. ρ is taken as the density of the lighter fluid, which is 1031.8 kg/m³. ∂s is taken as half of the fracture aperture, which is 2 mm, and $\partial \rho$ is taken as the density difference between the lighter and denser fluid, which is 79.2 kg/m³. Using these numbers, the smallest Ri in the system is estimated to be about 240. The values of Ri_c from previous studies range from 0.2 to 1.0 (Abarbanel et al., 1984; Galperin et al., 2007; Howard, 1961). Considering the Ri calculated in our system is 2 orders of magnitude larger than the reported values of Ri_c , the RTI appears to be the main mechanism that makes the runlet unstable.

3.4. Influence of Inertial Force

From Figure 9b, we observe that more stagnation points are present near the inlet, and the number decreases in the flow (vertical) direction. This is because more vortices appear at the lower part of the system due to the high

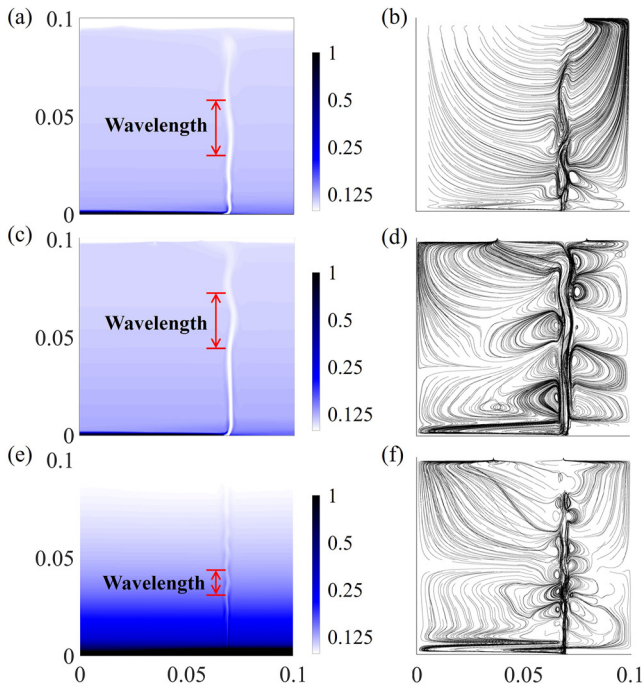


Figure 13. (a) Depth-averaged concentration distribution of the Case 10 that neglects inertial force. (b) Projected three-dimensional (3D) streamlines of the Case 10 that neglects inertial force. (c) Depth-averaged concentration distribution of the reference case. (d) Projected 3D streamlines of the reference case. (e) Depth-averaged concentration distribution of the Case 11, in which the injection rate of lighter fluid is 0.17 ml/min. (f) Projected 3D streamlines of the Case 11, in which the injection rate of lighter fluid is 0.17 ml/min.

concentration gradient near the inlet. As we discussed before, the spiral flow around vortices makes the runlet unstable. Intuitively, more vortices should lead to a more unstable runlet. However, in both experimental and simulation results (Figures 2b–2d), we observed that runlets are stable and straight near the injection point (lower part) and become unstable as the distance from the inlet increases. One reason for the stability may be due to the high inertial force of lighter fluid near the inlet, suppressing the effects of vortical flows. To investigate the influence of inertial force on the stability of the runlet, we considered Case 10 that solves Stokes equations instead of N-S equations to simulate noninertial flow. Stokes equations can be obtained by removing the inertial terms in the momentum balance Equation 2

$$\frac{\partial(\rho u)}{\partial t} = -\nabla p + \rho g + \rho \nu \nabla^2 u \quad (10)$$

After applying the Boussinesq approximation, Equation 9 can be written as

$$\rho_0 \frac{\partial u}{\partial t} = -\nabla p + \rho_0 \nu \nabla^2 u \quad (11)$$

The parameters of the fluid used in this case are the same as the reference case in Table 1. We compare this case (Case 10) with the reference case (Case 1) where we account for the inertial force. The concentration distributions and projected 3D streamlines of the case that neglect inertial force are shown in Figures 13a and 13b. Results show that in both cases, the upper half part of the runlet is unstable, and the wavelengths are similar. However, in the case that the inertial force is neglected, the instability initiates near the inlet, and the upward movements of vortices are limited, which is clearly different from the case considering the inertia (Movie S1). The results are consistent with the hypothesis that in the case considering the inertial force, although vortices emerge at the lower part of the system as predicted by the high Rayleigh number, the large inertial force caused by the fast runlet flow

maintains the straightness of the runlet near the inlet. As we discussed in Section 3.3, the vortices travel up along with the flow because of the injection force. In the upper part, due to the decrease in inertial force, the vortical flow effect dominates over the injection force, so the runlet shows enhanced fluctuations. In the case that neglects the inertial force, the vortices appearing at the lower part can lead to the fluctuation of the entire runlet, but the vortices show limited upward movement due to the lack of inertia force.

To further study the effects of inertial force on the runlet stability, we simulated Case 11 with a smaller injection rate of the lighter fluid than the reference case (Case 1). The inertial force increases as the injection rate increases. In Case 11 shown in Table 1, the injection rate of the lighter fluid is the same as the injection rate of the denser fluid, which is 0.17 ml/min, an order of magnitude smaller than the lighter fluid injection rate in the reference case. From the concentration distributions (Figure 13e) of Case 11, although the inertial force is smaller, the lower part of the runlet is still straight due to the inertial force. Further, the upper part of the runlet is unstable in both cases but the wavelength in Case 11 is significantly shorter than that in the reference case, which is consistent with what is observed in laboratory experiments (Xu et al., 2023). Studies on confined laminar impinging slot-jet also reported that the size of a vortex increases with increasing Reynolds number (Sexton et al., 2018; Sivasamy et al., 2007). From Case 11, we can conclude that the increase in injection rate of lighter fluid increases the wavelength of the runlet, which is associated with the size of vortices. These findings highlight that the inertia effect can be critical for fracture flows even in the laminar flow regimes.

3.5. Effects of Fracture Roughness and Aperture Variability

Fracture surfaces are rough in nature, and fracture roughness is known to significantly affect fluid flow and transport. For example, aperture variability due to surface roughness can lead to preferential flow paths and stagnation zones (Kang et al., 2016; Tsang & Neretnieks, 1998; Yoon & Kang, 2021). To study the effects of

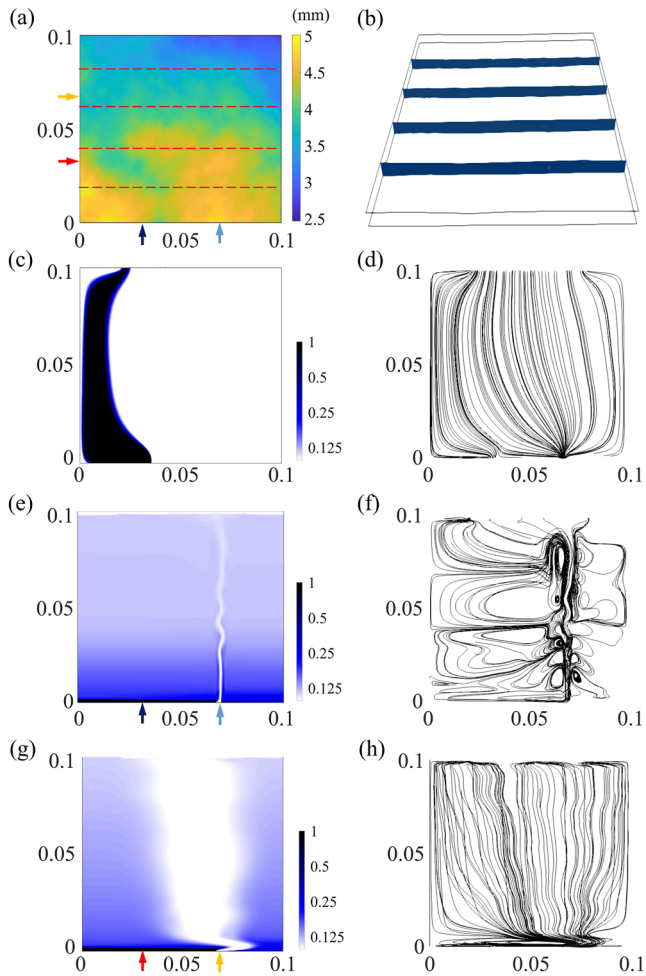


Figure 14. (a) Aperture map formed by two rough fracture surfaces. Dashed lines show cross-sectional locations. Blue arrow shows the injection position of lighter fluid in the Case 13. Orange arrow shows the injection position of lighter fluid in the Case 14. For the Case 14, we rotate the fracture to place the injection position at the bottom. (b) Cross-sections of the rough fracture. (c) Depth-averaged concentration distribution of the rough fracture case in which the two fluids have same density at three pore volume injection (PVI). (d) Projected three-dimensional (3D) streamlines in the rough fracture case in which the two fluids have same density at three PVI. (e) Depth-averaged concentration distribution of the Case 13 at three PVI. The unstable runlet is still evident in rough fracture. (f) Projected 3D streamlines of the Case 13 at three PVI. Note the vortices along the runlet. (g) Depth-averaged concentration distribution of the Case 14 at three PVI. The runlet is wider. (h) Projected 3D streamlines of the Case 14 at three PVI. The projected 3D streamlines are dispersed due to aperture variability. Cases 13 and 14 are based on the same rough fracture but the injection location is different.

surface roughness on runlet, we conducted 3D numerical simulations on a real rock fracture geometry (Cases 12–14). The surface topography data was obtained by scanning a natural fracture (Sawayama et al., 2021) and was used to generate a rough fracture. We chose an area of $100\text{mm} \times 100\text{mm}$ from the data set. Figure 14a shows the aperture map between the two rough fracture surfaces. The mechanical aperture (the average distance between the two fracture surfaces) is fixed to be 4 mm such that it is consistent with the cases with parallel plates. Figure 14b shows the cross-sections of the rough fracture at four different locations. Generally, the lower half of the fracture has larger aperture values than the upper half (Figure 14a).

To investigate density effects on runlet formation in rough fractures, we first simulated the case in which the two fluids have the same density (Case 12). The fluid properties we used in this case are the same as Case 2 (Table 1). No runlet is formed in the rough fracture without density contrast (Figures 14c and 14d), which confirms that the density contrast between two fluids injected is critical to the formation of the runlet also in a rough fracture. We then considered the case in which the two fluids have the density difference (Case 13). In Figure 14a, the blue arrow indicates the injection position of lighter fluid, and the black arrow indicates the injection position of denser fluid. The concentration distribution (Figure 14e) clearly shows that the runlet of lighter fluid is present and unstable in the rough fracture case. The 3D streamlines (Figure 14f) show that there are vortices along the runlet, and they cause the runlet to become unstable, similar to that observed in the uniform aperture fracture (i.e., parallel plates).

To further study the effects of fracture roughness on the formation and instability of the runlet, we simulated an additional case (Case 14) by rotating the fracture. For Case 14, the injection position of lighter fluid is indicated with the orange arrow, and the injection position of denser fluid is indicated with red arrow in Figure 14a. The result (Figures 14g and 14h) shows that the runlet formation is significantly different from Case 12. The concentration distribution (Figure 14g) shows that the width of the runlet is larger in Case 14. The increase in runlet width and area is attributed to the aperture variability. In Case 14, the right half of the fracture where the lighter fluid is injected has relatively smaller apertures, while the left half of the fracture where the denser fluid is injected has larger apertures. When the lighter fluid flows through the zone with narrower apertures, due to the mass conservation, the flow cross-sectional area of lighter fluid will likely increase. Therefore, in Case 14, the runlet width is larger. This is evident from the 3D streamlines (Figure 14h), in which we can observe how the streamlines are dispersed and tend to flow to the area with larger fracture aperture. Furthermore, the streamlines show that there is only one large stable vortex near the inlet that does not travel upwards. This indicates that the aperture variability can affect the movement of vortices. Results from this section confirm that a runlet still appears in rough fractures, but the shape and instability of runlet are sensitive to a given aperture field. In nature, fracture roughness and aperture can vary widely (Ogilvie et al., 2006; Zhang et al., 2019), and thus a more comprehensive study on runlet formation in rough fractures should be an important topic of future study.

4. Summary and Conclusions

In this study, we investigated variable-density flows in vertical fractures and elucidated the formation and origin of the unstable runlet based on a visual laboratory experiment and direct 3D numerical simulations. Results

show that when two fluids with different densities are injected at the bottom of a vertical fracture, the lighter fluid is confined to a narrow runlet which could be unstable. The formation of the runlet requires a sufficient density difference between the fluids, and the mixing of the two fluids is demonstrated to play an important role. If there is no density difference between the two fluids, or if the two fluids are well-mixed, the runlet does not appear.

We identified RTI as the origin of vortices that control the instability of the runlet. The large concentration gradient between the runlet and surrounding fluid, especially at the lower part of the fracture, leads to the emergence of vortices due to the RTI. The estimation of the critical Rayleigh number further confirmed that the instability arises due to the RTI: the estimated Rayleigh number near the inlet is larger than the critical Rayleigh number. Further, flow topology analysis of the velocity field identified vortices, which are shown to be strongly correlated with runlet instability. Vortices emerge due to the RTI near the inlet, and they are shown to travel along the runlet, controlling the runlet instability. The number of vortices over time showed a very similar trend to the time evolution of the runlet length.

Inertial force is shown to control the effect of vortices on runlet instability. Vortices emerge near the inlet, but high local inertial force near the inlet keeps the runlet straight. Due to the injection force, the vortices travel upwards with the flow. In the upper part, where the inertial (injection) force decreases, the vortical flows dominate the shaping of the runlet, making the runlet to be unstable. In the case without inertial force, the instability not only occurs in the upper part of the fracture, but also near the inlet. The vortices that appear near the inlet make the entire runlet become unstable due to the lack of inertia. The upward movements of vortices are limited due to the lack of inertia force, but their effects near the inlet affect the entire runlet. The injection rate of the lighter fluid is also shown to control the wavelength of the unstable runlet and the size of the vortices. When the injection rate is smaller, which means the inertial force is smaller, the wavelength and size of vortices are smaller. Our results highlight that even in laminar fracture flow conditions, inertia can play a critical role. Finally, we confirmed the formation of unstable runlets in rough fractures, and aperture variability is demonstrated to play an important role in shaping the runlet and its instability.

In this study, various factors affecting the formation and instability of a runlet in a vertical fracture were explored. The results of this study elucidate the underlying mechanisms triggering the instability in variable-density fracture flows and provide insights into the complex interplay between transport, mixing, and runlet instability in a vertical fracture. This study has important implications for the prediction, design, and operation of subsurface processes and applications that involve variable-density fluids in channel flows. For example, the unstable runlet may have strong impact on the extent of seawater intrusion in coastal aquifers. Further, runlets may have even more dramatic effects if dissolution and precipitation reactions are present. The locations of dissolution and precipitation will be a strong function of runlet characteristics, which may control the efficiency of geologic carbon mineralization. The effects of the runlet on dissolution and precipitation reactions in rough fractures is an important topic for future study.

Data Availability Statement

All simulation input files are available in Cao et al. (2023) through the Data Repository for University of Minnesota (DRUM).

References

- Abarbanel, H. D. I., Holm, D. D., Marsden, J. E., & Ratiu, T. (1984). Richardson number criterion for the nonlinear stability of three-dimensional stratified flow. *Physical Review Letters*, 52(26), 2352–2355. <https://doi.org/10.1103/PhysRevLett.52.2352>
- Ahoulou, A. W. A., Tinet, A. J., Oltéan, C., & Golfier, F. (2020). Experimental insights into the interplay between buoyancy, convection, and dissolution reaction. *Journal of Geophysical Research: Solid Earth*, 125, e2020JB020854. <https://doi.org/10.1029/2020JB020854>
- Al-Bahlani, A. M., & Babadagli, T. (2012). Visual analysis of diffusion process during oil recovery using a Hele-Shaw model with hydrocarbon solvents and thermal methods. *Chemical Engineering Journal*, 181–182, 557–569. <https://doi.org/10.1016/J.CEJ.2011.11.087>
- Almarcha, C., Trevelyan, P. M. J., Grosfils, P., & de Wit, A. (2010). Chemically driven hydrodynamic instabilities. *Physical Review Letters*, 104(4), 044501. <https://doi.org/10.1103/PhysRevLett.104.044501>
- Asimov, D. (1993). Notes on the topology of vector fields and flows. *Proceedings of IEEE Visualization*, 1–21.
- Bakker, P. G., & Berger, M. S. (1991). Bifurcations in flow patterns: Some applications of the qualitative theory of differential equations in fluid dynamics. In *Nonlinear topics in the mathematical sciences*. Springer. <https://doi.org/10.1007/978-94-011-3512-2>
- Bochet, O., Bethencourt, L., Dufresne, A., Farasin, J., Pédrot, M., Labasque, T., et al. (2020). Iron-oxidizer hotspots formed by intermittent oxic-anoxic fluid mixing in fractured rocks. *Nature Geoscience*, 13(2), 149–155. <https://doi.org/10.1038/s41561-019-0509-1>

Acknowledgments

PKK and HC acknowledge the support by the National Science Foundation under Grant EAR-2046015 and Grant CBET-2053413. We thank the Minnesota Supercomputing Institute (MSI) at the University of Minnesota for computational resources and support. LJP and XZ acknowledge support for the former Center for Nanoscale Controls on Geologic CO₂ (NCGC), an Energy Frontier Research Center funded by the U.S. Department of Energy, Office of Science, Basic Energy Sciences under Award DE-AC02-05CH11231.

- Bouquain, J., Meheust, Y., & Davy, P. (2011). Horizontal pre-asymptotic solute transport in a plane fracture with significant density contrasts. *Journal of Contaminant Hydrology*, 120–121, 184–197. <https://doi.org/10.1016/j.jconhyd.2010.08.002>
- Bresciani, E., Kang, P. K., & Lee, S. (2019). Theoretical analysis of groundwater flow patterns near stagnation points. *Water Resources Research*, 55, 1624–1650. <https://doi.org/10.1029/2018WR023508>
- Bujack, R., Tsai, K., Morley, S. K., & Bresciani, E. (2021). Open source vector field topology. *SoftwareX*, 15, 100787. <https://doi.org/10.1016/j.softx.2021.100787>
- Cao, H., Yoon, S., & Kang, P. K. (2023). Numerical simulation setup for variable-density flows in vertical fractures [Dataset]. University of Minnesota. <https://doi.org/10.13020/5V9X-W890>
- Cengel, Y., Turner, R., & Smith, R. (2001). Fundamentals of thermal-fluid sciences. *Applied Mechanics Reviews*, 54(6), B110–B112. <https://doi.org/10.1115/1.1421126>
- Chaudhuri, A., Rajaram, H., Viswanathan, H., Zvyoloslki, G., & Stauffer, P. (2009). Buoyant convection resulting from dissolution and permeability growth in vertical limestone fractures. *Geophysical Research Letters*, 36, L03401. <https://doi.org/10.1029/2008GL036533>
- Chen, J. D. (1989). Growth of radial viscous fingers in a Hele-Shaw cell. *Journal of Fluid Mechanics*, 201(1), 223–242. <https://doi.org/10.1017/S0022112089000911>
- Chiogna, G., Cirpka, O. A., Rolle, M., & Bellin, A. (2015). Helical flow in three-dimensional nonstationary anisotropic heterogeneous porous media. *Water Resources Research*, 51, 261–280. <https://doi.org/10.1002/2014WR015330>
- Cirpka, O. A., Chiogna, G., Rolle, M., & Bellin, A. (2015). Transverse mixing in three-dimensional nonstationary anisotropic heterogeneous porous media. *Water Resources Research*, 51, 241–260. <https://doi.org/10.1002/2014WR015331>
- Cohen, C., Berhanu, M., Derr, J., & Courrech Du Pont, S. (2020). Buoyancy-driven dissolution of inclined blocks: Erosion rate and pattern formation. *Physical Review Fluids*, 5(5), 053802. <https://doi.org/10.1103/PhysRevFluids.5.053802>
- Contreras, P. S., Speetjens, M. F. M., & Clercx, H. J. H. (2017). Lagrangian transport in a class of three-dimensional buoyancy-driven flows. *Journal of Fluid Mechanics*, 832, 5–40. <https://doi.org/10.1017/jfm.2017.680>
- de Anna, P., Le Borgne, T., Dentz, M., Tartakovsky, A. M., Bolster, D., & Davy, P. (2013). Flow intermittency, dispersion, and correlated continuous time random walks in porous media. *Physical Review Letters*, 110(18), 184502. <https://doi.org/10.1103/PhysRevLett.110.184502>
- de Barros, F. P. J., Dentz, M., Koch, J., & Nowak, W. (2012). Flow topology and scalar mixing in spatially heterogeneous flow fields. *Geophysical Research Letters*, 39, L08404. <https://doi.org/10.1029/2012GL051302>
- Déléry, J. (2013). *Three-dimensional separated flows topology: Singular points, beam splitters and vortex structures*. John Wiley & Sons.
- Dentz, M., Le Borgne, T., Englert, A., & Bijeljic, B. (2011). Mixing, spreading and reaction in heterogeneous media: A brief review. *Journal of Contaminant Hydrology*, 120–121, 1–17. <https://doi.org/10.1016/j.jconhyd.2010.05.002>
- Dietrich, P., Helmig, R., Sauter, M., Teutsch, G., Hötzl, H., & Köngeter, J. (2005). Flow and transport in fractured porous media. In *Flow and transport in fractured porous media* (pp. 1–447). Springer. <https://doi.org/10.1007/B138453>
- Fernandez, J., Kurowski, P., Petitjeans, P., & Meiburg, E. (2002). Density-driven unstable flows of miscible fluids in a Hele-Shaw cell. *Journal of Fluid Mechanics*, 451, 239–260. <https://doi.org/10.1017/s0022112001006504>
- Funada, T., & Joseph, D. D. (2001). Viscous potential flow analysis of Kelvin-Helmholtz instability in a channel. *Journal of Fluid Mechanics*, 445, 261–283. <https://doi.org/10.1017/s0022112001005572>
- Galperin, B., Sukoriansky, S., & Anderson, P. S. (2007). On the critical Richardson number in stably stratified turbulence. *Atmospheric Science Letters*, 8(3), 65–69. <https://doi.org/10.1002/asl.153>
- Gartling, D. K., & Hickox, C. E. (1985). A numerical study of the applicability of the Boussinesq approximation for a fluid-saturated porous medium. *International Journal for Numerical Methods in Fluids*, 5(11), 995–1013. <https://doi.org/10.1002/flid.1650051105>
- Globus, A., Levit, C., & Lasinski, T. (1991). A tool for visualizing the topology of three-dimensional vector fields. In *Proceedings of the 2nd Conference on Visualization 1991, VIS 1991* (pp. 33–40). <https://doi.org/10.1109/visual.1991.175773>
- Graf, T., & Therrien, R. (2005). Variable-density groundwater flow and solute transport in porous media containing nonuniform discrete fractures. *Advances in Water Resources*, 28(12), 1351–1367. <https://doi.org/10.1016/j.advwatres.2005.04.011>
- Graf, T., & Therrien, R. (2007). Variable-density groundwater flow and solute transport in irregular 2D fracture networks. *Advances in Water Resources*, 30(3), 455–468. <https://doi.org/10.1016/j.advwatres.2006.05.003>
- Gray, D. D., & Giorgini, A. (1976). The validity of the Boussinesq approximation for liquids and gases. *International Journal of Heat and Mass Transfer*, 19(5), 545–551. [https://doi.org/10.1016/0017-9310\(76\)90168-X](https://doi.org/10.1016/0017-9310(76)90168-X)
- Günther, A., & Jensen, K. F. (2006). Multiphase microfluidics: From flow characteristics to chemical and materials synthesis. *Lab on a Chip*, 6(12), 1487–1503. <https://doi.org/10.1039/B609851G>
- Hage, E., & Tilgner, A. (2010). High Rayleigh number convection with double diffusive fingers. *Physics of Fluids*, 22(7), 076603. <https://doi.org/10.1063/1.3464158>
- Hamimid, S., Guellal, M., & Bouafia, M. (2021). Limit of the buoyancy ratio in Boussinesq approximation for double-diffusive convection in binary mixture. *Physics of Fluids*, 33(3), 036101. <https://doi.org/10.1063/5.0037320>
- He, X., Zhang, R., Chen, S., & Doolen, G. D. (1999). On the three-dimensional Rayleigh-Taylor instability. *Physics of Fluids*, 11(5), 1143–1152. <https://doi.org/10.1063/1.869984>
- Helman, J., & Hesselink, L. (1989). Representation and display of vector field topology in fluid flow data sets. *Computer*, 22(8), 27–36. <https://doi.org/10.1109/2.35197>
- Hidalgo, J. J., & Dentz, M. (2018). Mixing across fluid interfaces compressed by convective flow in porous media. *Journal of Fluid Mechanics*, 838, 105–128. <https://doi.org/10.1017/jfm.2017.888>
- Howard, L. N. (1961). Note on a paper of John W. Miles. *Journal of Fluid Mechanics*, 10(4), 509. <https://doi.org/10.1017/S0022112061000317>
- Huang, J. M., Tong, J., Shelley, M., & Ristroph, L. (2020). Ultra-sharp pinnacles sculpted by natural convective dissolution. *Proceedings of the National Academy of Sciences of the United States of America*, 117(38), 23339–23344. <https://doi.org/10.1073/pnas.2001524117>
- Kang, P. K., Brown, S., & Juanes, R. (2016). Emergence of anomalous transport in stressed rough fractures. *Earth and Planetary Science Letters*, 454, 46–54. <https://doi.org/10.1016/j.epsl.2016.08.033>
- Kitanidis, P. K. (1994). The concept of the dilution index. *Water Resources Research*, 30(7), 2011–2026. <https://doi.org/10.1029/94WR00762>
- Kneafsey, T. J., & Pruess, K. (2010). Laboratory flow experiments for visualizing carbon dioxide-induced, density-driven brine convection. *Transport in Porous Media*, 82(1), 123–139. <https://doi.org/10.1007/s11242-009-9482-2>
- Kull, H. J. (1991). Theory of the Rayleigh-Taylor instability. *Physics Reports*, 206(5), 197–325. [https://doi.org/10.1016/0370-1573\(91\)90153-D](https://doi.org/10.1016/0370-1573(91)90153-D)
- Le Borgne, T., Dentz, M., Bolster, D., Carrera, J., De Dreuzy, J. R., & Davy, P. (2010). Non-Fickian mixing: Temporal evolution of the scalar dissipation rate in heterogeneous porous media. *Advances in Water Resources*, 33(12), 1468–1475. <https://doi.org/10.1016/j.advwatres.2010.08.006>
- Le Borgne, T., Dentz, M., & Villermaux, E. (2013). Stretching, coalescence, and mixing in porous media. *Physical Review Letters*, 110(20), 204501. <https://doi.org/10.1103/PhysRevLett.110.204501>

- Lee, S. H., & Kang, P. K. (2020). Three-dimensional vortex-induced reaction hot spots at flow intersections. *Physical Review Letters*, *124*(14), 144501. <https://doi.org/10.1103/PhysRevLett.124.144501>
- Le Quere, P. (1990). A note on multiple and unsteady solutions in two-dimensional convection in a tall cavity. Retrieved from http://asmedigitalcollection.asme.org/heattransfer/article-pdf/112/4/965/5651934/965_1.pdf
- Lester, D. R., Metcalfe, G., Trefry, M. G., Ord, A., Hobbs, B., & Rudman, M. (2009). Lagrangian topology of a periodically reoriented potential flow: Symmetry, optimization, and mixing. *Physical Review E*, *80*(3), 036208. <https://doi.org/10.1103/PhysRevE.80.036208>
- Morijiri, T., Sunahiro, S., Senaha, M., Yamada, M., & Seki, M. (2011). Sedimentation pinched-flow fractionation for size- and density-based particle sorting in microchannels. *Microfluidics and Nanofluidics*, *11*(1), 105–110. <https://doi.org/10.1007/S10404-011-0785-6/TABLES/2>
- Ogilvie, S. R., Isakov, E., & Glover, P. W. J. (2006). Fluid flow through rough fractures in rocks. II: A new matching model for rough rock fractures. *Earth and Planetary Science Letters*, *241*(3–4), 454–465. <https://doi.org/10.1016/j.epsl.2005.11.041>
- Oltéan, C., Golfier, F., & Buès, M. A. (2013). Numerical and experimental investigation of buoyancy-driven dissolution in vertical fracture. *Journal of Geophysical Research: Solid Earth*, *118*, 2038–2048. <https://doi.org/10.1002/jgrb.50188>
- Ott, H., & Oedai, S. (2015). Wormhole formation and compact dissolution in single- and two-phase CO₂-brine injections. *Geophysical Research Letters*, *42*, 2270–2276. <https://doi.org/10.1002/2015GL063582>
- Park, H. Y., Jang, K., Ju, J. W., & Yeo, I. W. (2012). Hydrogeological characterization of seawater intrusion in tidally-forced coastal fractured bedrock aquifer. *Journal of Hydrology*, *446–447*, 77–89. <https://doi.org/10.1016/j.jhydrol.2012.04.033>
- Perko, L. (2001). *Differential equations and dynamical systems* (3rd ed.). Springer.
- Perry, A. E., & Chong, M. S. (1994). Topology of flow patterns in vortex motions and turbulence. *Applied Scientific Research*, *53*(3–4), 357–374. <https://doi.org/10.1007/bf00849110>
- Perry, A. E., & Fairlie, B. D. (1975). Critical points in flow patterns. *Advances in Geophysics*, *18*(PB), 299–315. [https://doi.org/10.1016/S0065-2687\(08\)60588-9](https://doi.org/10.1016/S0065-2687(08)60588-9)
- Portarapillo, M., & di Benedetto, A. (2021). Risk assessment of the large-scale hydrogen storage in salt caverns. *Energies* *2021*, *14*(10), 2856. <https://doi.org/10.3390/EN14102856>
- Romanò, F., Albensoeder, S., & Kuhlmann, H. C. (2017). Topology of three-dimensional steady cellular flow in a two-sided anti-parallel lid-driven cavity. *Journal of Fluid Mechanics*, *826*, 302–334. <https://doi.org/10.1017/jfm.2017.422>
- Ronen, D., Yechieli, Y., & Kribus, A. (1995). Buoyancy-induced flow of a tracer in vertical conduits. *Water Resources Research*, *31*(5), 1167–1173. <https://doi.org/10.1029/95WR00201>
- Saffman, P. G., & Taylor, G. I. (1958). The penetration of a fluid into a porous medium or Hele-Shaw cell containing a more viscous liquid. *Proceedings of the Royal Society of London. Series A. Mathematical and Physical Sciences*, *245*(1242), 312–329. <https://doi.org/10.1098/rspa.1958.0085>
- Sawayama, K., Ishibashi, T., Jiang, F., Tsuji, T., Nishizawa, O., & Fujimitsu, Y. (2021). Scale-independent relationship between permeability and resistivity in mated fractures with natural rough surfaces. *Geothermics*, *94*, 102065. <https://doi.org/10.1016/j.geothermics.2021.102065>
- Sexton, A., Punch, J., Stafford, J., & Jeffers, N. (2018). The thermal and hydrodynamic behaviour of confined, normally impinging laminar slot jets. *International Journal of Heat and Mass Transfer*, *123*, 40–53. <https://doi.org/10.1016/j.ijheatmasstransfer.2018.02.083>
- Sharp, D. H. (1984). An overview of Rayleigh-Taylor instability. *Physica D: Nonlinear Phenomena*, *12*(1–3), 3–18. [https://doi.org/10.1016/0167-2789\(84\)90510-4](https://doi.org/10.1016/0167-2789(84)90510-4)
- Shikaze, S. G., Sudicky, E. A., & Schwartz, F. W. (1998). Density-dependent solute transport in discretely-fractured geologic media: Is prediction possible? *Journal of Contaminant Hydrology*, *34*(3), 273–291. [https://doi.org/10.1016/S0169-7722\(98\)00080-1](https://doi.org/10.1016/S0169-7722(98)00080-1)
- Simmons, C. T. (2005). Variable density groundwater flow: From current challenges to future possibilities. *Hydrogeology Journal*, *13*(1), 116–119. <https://doi.org/10.1007/s10040-004-0408-3>
- Sivasamy, A., Selladurai, V., & Rajesh Kanna, P. (2007). Numerical simulation of two-dimensional laminar slot-jet impingement flows confined by a parallel wall. *International Journal for Numerical Methods in Fluids*, *55*(10), 965–983. <https://doi.org/10.1002/flid.1492>
- Ślęzak, A., Dworecki, K., Jasik-Ślęzak, J., & Wasik, J. (2004). Method to determine the critical concentration Rayleigh number in isothermal passive membrane transport processes. *Desalination*, *168*(1–3), 397–412. <https://doi.org/10.1016/j.desal.2004.07.027>
- Smyth, W. D., & Moum, J. N. (2012). Ocean mixing by Kelvin-Helmholtz instability. *Oceanography*, *25*(2), 140–149. <https://doi.org/10.5670/oceanog.2012.49>
- Snippe, J., Gdanski, R., & Ott, H. (2017). Multiphase modelling of wormhole formation in carbonates by the injection of CO₂. *Energy Procedia*, *114*, 2972–2984. <https://doi.org/10.1016/j.egypro.2017.03.1426>
- Solano, T., Ordóñez, J. C., & Shoale, K. (2022). Natural convection in vertical enclosures with conjugate boundary conditions. *Journal of Fluid Mechanics*, *946*, A17. <https://doi.org/10.1017/jfm.2022.568>
- Stein, R. F., Nordlund, A., Stein, R. F., & Nordlund, A. (1989). Topology of convection beneath the solar surface. *The Astrophysical Journal*, *342*, L95–L98. <https://doi.org/10.1086/185493>
- Tenchine, S., & Gouze, P. (2005). Density contrast effects on tracer dispersion in variable aperture fractures. *Advances in Water Resources*, *28*(3), 273–289. <https://doi.org/10.1016/j.advwatres.2004.10.009>
- Theisel, H., Rössl, C., & Weinkauff, T. (2008). Topological representations of vector fields. In L. De Floriani, & M. Spagnuolo (Eds.) *Shape analysis and structuring. Mathematics and visualization* (pp. 215–240). Springer. https://doi.org/10.1007/978-3-540-33265-7_7
- Theisel, H., Weinkauff, T., Hege, H. C., & Seidel, H. P. (2005). Topological methods for 2D time-dependent vector fields based on stream lines and path lines. *IEEE Transactions on Visualization and Computer Graphics*, *11*(4), 383–394. <https://doi.org/10.1109/TVCG.2005.68>
- Tongwa, P., Nygaard, R., Blue, A., & Bai, B. (2013). Evaluation of potential fracture-sealing materials for remediating CO₂ leakage pathways during CO₂ sequestration. *International Journal of Greenhouse Gas Control*, *18*, 128–138. <https://doi.org/10.1016/j.ijggc.2013.06.017>
- Trevelyan, P. M. J., Almarach, C., & de Wit, A. (2011). Buoyancy-driven instabilities of miscible two-layer stratifications in porous media and Hele-Shaw cells. *Journal of Fluid Mechanics*, *670*, 38–65. <https://doi.org/10.1017/S0022112010005008>
- Tryggvason, G. (1988). Numerical simulations of the Rayleigh-Taylor instability. *Journal of Computational Physics*, *75*(2), 253–282. [https://doi.org/10.1016/0021-9991\(88\)90112-X](https://doi.org/10.1016/0021-9991(88)90112-X)
- Tsang, C. F., & Neretnieks, I. (1998). Flow channeling in heterogeneous fractured rocks. *Reviews of Geophysics*, *36*(2), 275–298. <https://doi.org/10.1029/97RG03319>
- Weinkauff, T. (2008). *Extraction of topological structures in 2D and 3D vector fields* (Doctoral thesis). University Magdeburg. Retrieved from <http://tinoweinkauff.net/publications/absweinkauff08phd.html>
- Weller, H. G., Tabor, G., Jasak, H., & Fureby, C. (1998). A tensorial approach to computational continuum mechanics using object-oriented techniques. *Computers in Physics*, *12*(6), 620–631. <https://doi.org/10.1063/1.168744>
- Wood, B. D., He, X., & Apte, S. V. (2020). Modeling turbulent flows in porous media. *Annual Review of Fluid Mechanics*, *52*(1), 171–203. <https://doi.org/10.1146/annurev-fluid-010719-060317>

- Wooding, R. A., Tyler, S. W., & White, I. (1997). Convection in groundwater below an evaporating salt lake: 1. Onset of instability. *Water Resources Research*, 33(6), 1199–1217. <https://doi.org/10.1029/96WR03533>
- Xu, Z., Cao, H., Yoon, S., Kang, P. K., Jun, Y., Kneafsey, T., et al. (2023). Gravity-driven controls on fluid and carbonate precipitate distributions in fractures. *Scientific Reports*, 13(1), 9400. <https://doi.org/10.1038/s41598-023-36406-8>
- Yamato, P., Tartèse, R., Duretz, T., & May, D. A. (2012). Numerical modelling of magma transport in dykes. *Tectonophysics*, 526–529, 97–109. <https://doi.org/10.1016/j.tecto.2011.05.015>
- Yoon, S., Dentz, M., & Kang, P. K. (2021). Optimal fluid stretching for mixing-limited reactions in rough channel flows. *Journal of Fluid Mechanics*, 916, A45. <https://doi.org/10.1017/jfm.2021.208>
- Yoon, S., & Kang, P. K. (2021). Roughness, inertia, and diffusion effects on anomalous transport in rough channel flows. *Physical Review Fluids*, 6(1), 014502. <https://doi.org/10.1103/PhysRevFluids.6.014502>
- Zalts, A., el Hasi, C., Rubio, D., Ureña, A., & D'Onofrio, A. (2008). Pattern formation driven by an acid-base neutralization reaction in aqueous media in a gravitational field. *Physical Review E-Statistical, Nonlinear and Soft Matter Physics*, 77(1), 015304. <https://doi.org/10.1103/PhysRevE.77.015304>
- Zhang, M., Prodanović, M., Mirabolghasemi, M., & Zhao, J. (2019). 3D microscale flow simulation of shear-thinning fluids in a rough fracture. *Transport in Porous Media*, 128(1), 243–269. <https://doi.org/10.1007/s11242-019-01243-9>